

Electrical capacitance tomography image reconstruction based on iterative Tikhonov regularization improved algorithm^{*}

YAN Chunman^{**} and ZOU Meng

School of Physics and Electronic Engineering, Northwest Normal University, Lanzhou 730070, China

(Received 4 April 2023; Revised 4 June 2023)

©Tianjin University of Technology 2023

Aiming at the problems of low reconstruction quality, poor robustness, and the inability to quickly and stably converge caused by the ill-posedness of electrical capacitance tomography image reconstruction, an improved algorithm based on iterative Tikhonov regularization (ITR) was proposed. The algorithm constructs a new objective function by introducing the L_p norm to carry out multi-criteria constraints, and introduces the result of the corrected Tikhonov regularization (TR) algorithm into the image reconstruction process together with the logarithmic weight factor as the estimated value. At the same time, an acceleration strategy is used, and the residual term is exponentially filtered. Perform ablation, initial value sensitivity, convergence, and noise interference experiments on the improved algorithm and compare it with other common algorithms. Experimental results show that the improved algorithm can quickly and stably converge and has good robustness and initial value insensitivity. The reconstructed image quality is high, the average correlation coefficient (CC) can reach 0.963 3, and the average relative error (RE) can be reduced to 0.069 4.

Document code: A **Article ID:** 1673-1905(2023)12-0762-7

DOI <https://doi.org/10.1007/s11801-023-3061-6>

Electrical capacitance tomography (ECT) is an essential subfield of process tomography (PT)^[1], which is based on computed tomography (CT). The majority of ECT measurement objects are multiphase flows. Similarly, ECT technology has been widely developed and implemented due to its excellent security, non-invasive visual measurement, and low cost^[2-4]. Examples include gas fluidized bed measuring, flame structure identification, and non-destructive tree inspection.

ECT technology is mainly divided into forward problems and inverse problems. ECT image reconstruction is a process for solving the inverse problem of ECT. The solution to the inverse problem of ECT is to restore the dielectric constant distribution in the field according to a certain image reconstruction algorithm by measuring the capacitance values between all electrode pairs and the sensitivity distribution obtained from the forward problem, and reconstruct the flow pattern in the form of an image. However, due to the non-uniqueness and instability of the solution, the ECT inverse problem is inevitably ill-posed^[5]. In the measurement, due to the inevitability of the existence of the medium in the field, the existence of the solution can be guaranteed. However, in practical applications, due to the limitations of sensor design and application scenarios, the projected value of the actual capacitance measurement is much smaller than the num-

ber of pixels required to reconstruct the image, so this problem is an underdetermined problem, and the solution is not unique, resulting in poor image quality in reconstruction. Due to the "soft field" problem of ECT, the sensitivity distribution in the field is affected by the distribution of the medium and has a nonlinear relationship. When the capacitive signal is slightly disturbed, the image will change greatly, so the solution is not stable, which makes it difficult to quickly and stably converge, and the robustness is poor. Due to the ill-posed nature of ECT image reconstruction, it is difficult to achieve satisfactory results in reconstructed images. Therefore, more and more ECT reconstruction algorithms have been proposed by researchers. Currently, image reconstruction algorithms are primarily categorized into three groups: direct algorithms, iterative algorithms, and intelligent algorithms. Common direct algorithms include the linear back projection (LBP) algorithm^[6], the Tikhonov regularization (TR) algorithm^[7,8], etc. Although the direct algorithm has a simple structure, low calculation, and fast imaging speed, its imaging accuracy is relatively low. Compared to the direct algorithm, the iterative algorithm has enhanced image quality. Such as the Landweber algorithm^[9], the iterative Tikhonov regularization (ITR) algorithm^[7], etc, but they are still limited by the defects of semi-convergence and slow convergence. In

^{*} This work has been supported by the National Natural Science Foundation of China (No.61961037), and the Gansu Provincial Department of Education 2021 Industry Support Program (No.2021CYZC-30).

^{**} E-mail: yancm2022@163.com

recent years, an intelligent algorithm based on neural network^[10] has also been proposed, but its development is also limited by the difficulty of obtaining training samples. Algorithms such as LBP and Landweber are not supported by prior information. Although the TR and ITR algorithms have prior information, a single piece of prior information is not enough to guarantee the quality of the reconstructed image. Therefore, more prior information is needed to better support the process of reconstructing images. And because the TR algorithm can effectively solve the inverse problem and has better stability, in recent years, researchers have proposed new objective functions based on the TR framework for complete image reconstruction. For example, the L_1 or L_2 norm is deployed as a fidelity item, and the L_1 norm, L_p norm, nuclear norm, etc are deployed independently or combined as regularization items^[11-13], etc.

Based on the above analysis, the article proposes a new objective function. The L_p norm is introduced on the basis of ITR, which can better balance the smoothness problem caused by the L_2 norm while increasing the sparsity of the solution. The prior image estimation information obtained by the corrected TR algorithm and the logarithmic weight factor are added to the solution process of the new objective function. At the same time, an acceleration strategy is introduced, and the iterative residual term is exponentially filtered. In order to verify the effectiveness of the improved algorithm, ablation experiments are carried out and compared with common algorithms. Experimental results show that regardless of subjective quality or objective indicators, the reconstruction quality of the improved algorithm is better than that of other comparison algorithms. In order to further verify the practical application value of the algorithm proposed in this paper, initial value, convergency, and noise interference experiments are carried out. The experimental results show that the algorithm in this paper can converge quickly and stably and has better initial value insensitivity and robustness.

ECT image reconstruction is the process of solving the ECT inverse problem. In the inverse problem, there is a nonlinear relationship between the capacitance and permittivity distribution between electrode pairs, which can be expressed as

$$C = F(\varepsilon). \quad (1)$$

Using Taylor expansion of the above equation and ignoring higher order terms, we can obtain

$$\Delta C = \frac{dF}{d\varepsilon}(\Delta\varepsilon). \quad (2)$$

Define $\frac{dF}{d\varepsilon}$ as the Jacobian matrix in continuous form,

and discretize and normalize it to obtain

$$\lambda = S \cdot g, \quad (3)$$

where λ is the normalized capacitance vector of m capacitance values measured by the ECT system, g is the n -dimensional permittivity distribution vector, and S is the sensitivity distribution matrix, that is, the

$m \times n$ -dimensional normalized sensitivity matrix. The paper uses an 8-electrode ECT sensor, and marks 1, 2...8 with any electrode as the starting point. First, apply an excitation electrode to electrode 1, give it a fixed voltage U , and then use electrodes 2, 3...8 as receiving electrodes to measure the capacitance values between 1—2, 1—3,...1—8, respectively, and so on until the No.8 electrode is measured, and a total of $m = C_8^2 = 28$ capacitance values can be detected. The paper uses triangles to divide the ECT sensor area into units, and divides $n=3$ 228 effective areas of imaging units. The dissection diagram is shown in Fig.1.

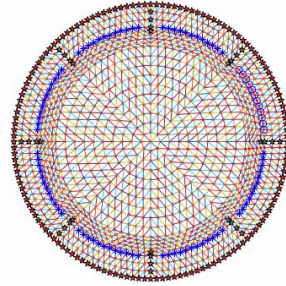


Fig.1 Triangulation results of ECT sensor field

Because the ECT inverse problem (image reconstruction) is ill-posed, it is difficult to solve Eq.(3) in real life. The TR method can better transform the ill-posed problem into the optimization problem of the objective function for solving, so it has been widely used. It is represented as follows

$$\min_g \{P(g) + \sum_{i=1}^n \mu_i \Omega_i(g)\}, \quad (4)$$

where $P(g)$ is the fidelity term, which is a measure of the accuracy of the solution. $\mu \geq 0$ is called the regularization parameter. $\Omega_i(g)$ is a regularization term.

The TR method takes the cost function of the least squares method as $P(g)$ items, and introduces the L_2 norm into $\Omega_i(g)$ items to form the objective function, which is expressed as follows

$$\min_g \{\|Sg - \lambda\|_2^2 + \mu \|L(g - \bar{g})\|_2^2\}, \quad (5)$$

where L is a matrix corresponding to a certain operation, which is usually set as the identity matrix I . \bar{g} is the estimated value of the solution obtained by some prior knowledge, and it is generally set to 0. According to the gradient of the objective function, the solution of the standard TR method can be expressed as

$$g = (S^T S + \mu I)^{-1} \cdot S^T \lambda. \quad (6)$$

In order to further improve the TR method, the ITR method was proposed. Eq.(6) is improved to be

$$\begin{cases} g_k = g_{k-1} + (S^T S + \mu I)^{-1} S^T r_{k-1}, k = 1, 2, \dots \\ r_k = \lambda - Sg_k \end{cases} \quad (7)$$

The value of the regularization parameter is more important, but because it requires a lot of calculations to get a suitable value, it is still based on empirical selection

in practical applications.

Although the ITR method can effectively solve the ill-posed problem and has good stability, its effect is smooth and the image quality is poor. To solve this problem, based on the ITR framework structure combined with Eq.(4), a new multi-regularized prior knowledge-constrained objective function is proposed, expressed as follows

$$\min_{\mathbf{g}} \{P(\mathbf{g}) + \mu_1 \Omega_1(\mathbf{g}) + \mu_2 \Omega_2(\mathbf{g})\}. \quad (8)$$

Deploy the L_2 norm as a fidelity term, which is expressed as follows

$$P(\mathbf{g}) = \|\mathbf{S}\mathbf{g} - \boldsymbol{\lambda}\|_2^2. \quad (9)$$

The design of the regularization term is crucial to improving the image's quality after reconstruction. A single piece of prior information is not enough to guarantee the quality of image reconstruction; therefore, multiple pieces of prior knowledge are needed to support it. First, deploy the L_2 norm as the regularization term of the first part, which is expressed as follows

$$\Omega_1(\mathbf{g}) = \|\mathbf{L}(\mathbf{g} - \gamma \bar{\mathbf{g}})\|_2^2. \quad (10)$$

The solution obtained by the TR algorithm is used as the estimated value of $\bar{\mathbf{g}}$, and γ is the correction parameter.

Secondly, in order to balance the problem that the L_2 norm imaging is too smooth and cannot better preserve the image detail information, the L_p norm is introduced. Studies have demonstrated that the L_p norm can significantly reduce the number of pixels necessary for reconstruction and produce a sparser solution than the L_1 and L_2 norms^[14]. The second part of the regularization term is expressed as

$$\Omega_2(\mathbf{g}) = \|\mathbf{g}\|_p. \quad (11)$$

According to Eqs.(9), (10), (11) and (4), the new objective function can be obtained, expressed as follows

$$\min_{\mathbf{g}} \left\{ \|\mathbf{S}\mathbf{g} - \boldsymbol{\lambda}\|_2^2 + \mu(\|\mathbf{L}(\mathbf{g} - \gamma \bar{\mathbf{g}})\|_2^2 + \|\mathbf{g}\|_p) \right\}. \quad (12)$$

If μ is small, the new problem constructed is too close to the original problem and cannot be regularized. On the contrary, although the stability can be improved, it deviates from the original problem and produces an invalid solution^[15]. This paper selects 0.02 as the regularization parameter based on experience.

To facilitate the implementation of the algorithm more easily^[15], $\|\mathbf{g}\|_p$ can be approximated as $\|\boldsymbol{\psi}\mathbf{g}\|_2^2$. $\boldsymbol{\psi}$ is a diagonal matrix with $\beta(|\mathbf{g}_k| + \tau)^{-1+p/2}$ diagonal elements, β is a correction parameter, and 0.001 is selected according to experience. $p \in [0, 1]$, τ takes a very small value.

Finding the conjugate gradient of the objective function, let $\nabla \min = 0$, which is expressed as follows

$$(\mathbf{S}^T \mathbf{S} + \mu \boldsymbol{\psi}^T \boldsymbol{\psi} + \mu \mathbf{L}^T \mathbf{L}) \mathbf{g} = \mathbf{S}^T \boldsymbol{\lambda} + \mu \mathbf{L}^T \mathbf{L} \gamma \bar{\mathbf{g}}. \quad (13)$$

To improve the image quality following reconstruction, \mathbf{L} in the formula is improved on the basis of \mathbf{I} ,

namely $\mathbf{L} = \mathbf{I} + \boldsymbol{\psi}$. Let $\mathbf{w} = \mathbf{S}^T \mathbf{S} + \mu \boldsymbol{\psi}^T \boldsymbol{\psi} + \mu \mathbf{L}^T \mathbf{L}$, $\mathbf{T} = \mathbf{L}^T \mathbf{L}$, which can be expressed as follows

$$\mathbf{g} = \mathbf{w}^{-1} (\mathbf{S}^T \boldsymbol{\lambda} + \mu \mathbf{T} \gamma \bar{\mathbf{g}}). \quad (14)$$

From the perspective of stable convergence of the algorithm, the logarithmic weight factor mechanism is used to search for the global optimal and then search for the local optimal direction to iterate. Combining Eqs.(3) and (14), the revised formula is updated as follows

$$\begin{cases} \mathbf{g}_k = \ln \delta \mathbf{g}_{k-1} + \partial \mathbf{w}^{-1} (\mathbf{S}^T \mathbf{r}_{k-1} + \mu \mathbf{T} \gamma \bar{\mathbf{g}}), \\ \mathbf{r}_k = \mathbf{r}_k + \partial (\boldsymbol{\lambda} - \mathbf{S} \mathbf{g}_k) \end{cases}, k=1, 2, \dots, (15)$$

where δ is the weight factor, after a lot of repeated experiments, when $\delta \in (2.7, 2.9)$ is more ideal. ∂ is the relaxation factor.

In order to further improve the quality of image reconstruction, this paper introduces an exponential filter function to the residual vector \mathbf{r}_k ^[16]. In the discrete state, the bilateral sequence exponential filter $h(n)$ is

$$h(n) = e^{-\eta} h_+(n-1) + kx(n) + e^{-\eta} h_-(n-1) + ke^{-\eta} x(n+1), \quad (16)$$

where k is the order of the exponential filter. η is the filter parameter, which is taken as 0.000 1. Let $k=0$, combined with Eq.(15), the reconstruction formula of the improved algorithm in this paper can be described as

$$\begin{cases} \mathbf{g}_k = \ln \delta \mathbf{g}_{k-1} + \partial \mathbf{w}^{-1} (\mathbf{S}^T \mathbf{r}_{k-1} + \mu \mathbf{T} \gamma \bar{\mathbf{g}}), \\ \mathbf{r}_k = e^{-\eta} (\mathbf{r}_k + \partial (\boldsymbol{\lambda} - \mathbf{S} \mathbf{g}_k)) \end{cases}, k=1, 2, \dots, (17)$$

After a lot of repeated experiments, $\partial \in (1.0, 1.4)$ is more ideal.

In order to improve the speed of image reconstruction, introduce an acceleration strategy^[17] to achieve fast convergence. Finally, its iterative formula is updated as

$$\begin{cases} \mathbf{l}_k = \ln \delta \mathbf{g}_{k-1} + \partial \mathbf{w}^{-1} (\mathbf{S}^T \mathbf{r}_{k-1} + \mu \mathbf{T} \gamma \bar{\mathbf{g}}), \\ \mathbf{r}_k = e^{-\eta} (\mathbf{r}_k + \partial (\boldsymbol{\lambda} - \mathbf{S} \mathbf{g}_k)) \end{cases}, k=1, 2, \dots, (18)$$

$$t_k = \frac{1}{2} \left(1 + \sqrt{1 + 4t_{k-1}^2} \right), \quad (19)$$

$$\mathbf{g}_k = \mathbf{l}_k + (t_{k-1} - 1/t_k)(\mathbf{l}_k - \mathbf{l}_{k-1}), \quad (20)$$

where t_k is the parameter used for the acceleration step, $t_0=1$. Using the acceleration strategy can make the algorithm converge quickly and stably, and reduce the amount of calculation.

ECT image reconstruction was completed on a computer with an Intel(R) Core(TM) i5-7500 3.40 GHz CPU and 16 GB memory. In order to verify the imaging capability of the improved algorithm, LBP, TR, TSVD, ART, Landweber, ITR, and the improved algorithm were selected for comparative experiments. In the experiment, four common two-phase simulated flow patterns were selected as the research objects: core flow, bubble flow, circular flow, and laminar flow (respectively designated as flow patterns a, b, c, and d). To evaluate the imaging performance of the improved algorithm, it primarily conducts ablation, initial value, convergency, and noise interference experiments and compares it to other prevalent methods.

In order to quantitatively evaluate the quality of reconstructed images, the relative error (RE) and correlation coefficient (CC) are used as evaluation criteria, which are expressed as follows

$$RE = \frac{\|\mathbf{g} - \hat{\mathbf{g}}\|}{\|\hat{\mathbf{g}}\|}, \quad (21)$$

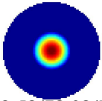
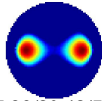
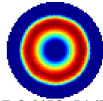
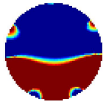
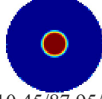
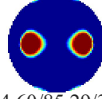

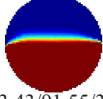

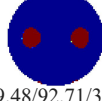

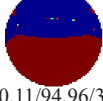
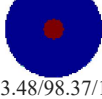


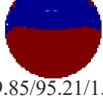
$$CC = \frac{\sum_{i=1}^D (\mathbf{g}_i - \bar{\mathbf{g}})(\hat{\mathbf{g}}_i - \bar{\hat{\mathbf{g}}})}{\sqrt{\sum_{i=1}^D (\mathbf{g}_i - \bar{\mathbf{g}})^2 \sum_{i=1}^D (\hat{\mathbf{g}}_i - \bar{\hat{\mathbf{g}}})^2}}, \quad (22)$$

where \mathbf{g} represents the permittivity distribution obtained by the image reconstruction algorithm, $\hat{\mathbf{g}}$ is the true permittivity distribution in the pipeline, $\bar{\mathbf{g}}$ and $\bar{\hat{\mathbf{g}}}$ are

the average values of \mathbf{g} and $\hat{\mathbf{g}}$ respectively, and D is the dimension of \mathbf{g} and $\hat{\mathbf{g}}$. When the RE is smaller and the CC is larger, it means that the quality of the reconstructed image is higher.

In order to visually verify the image reconstruction effect of the improved algorithm, ablation experiments are carried out on the improved algorithm. The results are shown in Tab.1. The selection of iteration times is determined by numerical experiments. Part A represents the application of the newly proposed objective function. Part B represents the exponential filtering of the residual term. Part C represents the introduction of the acceleration strategy. T represents the reconstruction time.

Tab.1 Results of ablation experiment

ITR	A	B	C	Flow pattern a RE (%) / CC (%) / T (s)	Flow pattern b RE (%) / CC (%) / T (s)	Flow pattern c RE (%) / CC (%) / T (s)	Flow pattern d RE (%) / CC (%) / T (s)
✓				 13.52/78.02/71.48	 15.29/80.48/73.17	 37.26/53.51/71.02	 20.57/79.57/75.66
✓	✓			 10.45/87.95/3.03	 14.60/85.29/3.67	 14.99/86.52/3.08	 13.43/91.55/3.04
✓	✓	✓		 9.28/89.61/3.08	 9.48/92.71/3.65	 8.14/95.53/4.04	 10.11/94.96/3.59
✓	✓	✓	✓	 3.48/98.37/1.79	 8.33/94.31/1.99	 6.11/97.43/1.98	 9.85/95.21/1.96

It can be seen from Tab.1 that when parts A, B, and C are integrated in turn, the objective indicators and subjective quality are significantly improved. In terms of objective indicators, when parts A, B, and C are integrated in sequence, the average RE drops to about 0.133 7, 0.092 5, and 0.069 4, respectively. Compared with the ITR algorithm, it is about 38.27%, 57.29%, and 67.96% lower, respectively. The average CC can reach about 0.878 3, 0.932 0, and 0.963 3, respectively, which is about 20.48%, 27.85%, and 32.14% higher than the ITR algorithm. Compared with the ITR algorithm, the reconstruction time of the improved algorithm is also reduced, with an average of about 1.93 s. In terms of subjective quality, when part A is integrated, the quality of the reconstructed image is significantly improved, but there are still artifacts, and the details and edge information are not clear. When integrated into part B, the reconstructed image's artifacts and detail information are greatly enhanced, but the edge information is still biased and there are a small amount of artifacts. When integrated into part C, the artifacts of the reconstructed image are eliminated, the details and edge information can be better preserved, and the reconstructed image is closer to the original flow pattern. Thus, the efficacy of the im-

proved algorithm has been confirmed.

In order to quantitatively evaluate the quality of the reconstructed image, this paper compares the objective indicators RE and CC of each algorithm, and the results.

In Tabs.2 and 3, a, b, c, and d represent four flow patterns. In this paper, the truncation parameter of the TSVD algorithm in the comparison algorithm is selected as 0.02^[11]. The regularization parameters of both the TR algorithm and the ITR algorithm are selected as 0.000 01^[9]. The iterative algorithm is iterated 100 times to reconstruct the image. From Tabs.2 and 3, for the reconstruction of the four flow patterns, the RE of the improved algorithm is 0.039 5, 0.083 2, 0.061 2, and 0.099 7, which is about 52.81%, 34.44%, 75.32%, and 68.07% lower than the ITR, respectively. CC is 0.982 1, 0.943 3, 0.974 2, and 0.950 9 in turn, which are respectively 5.64%, 9.28%, 44.48%, and 85.11% higher than ITR. The objective index of the improved algorithm is better than other algorithms, which verifies the effectiveness of the algorithm and proves that the quality of the reconstructed image is high.

In order to compare the imaging effect of each algorithm more subjectively, the subjective quality of images reconstructed by each algorithm is compared, and the

results are shown in Tab.4.


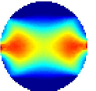
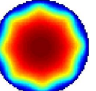
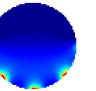
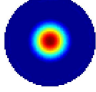
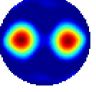
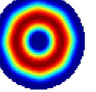
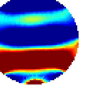
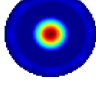
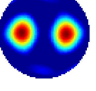
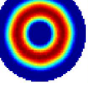
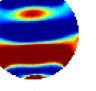
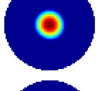
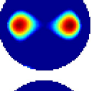
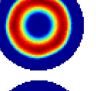

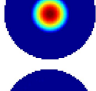
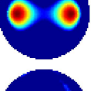
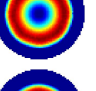

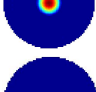
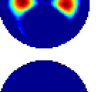
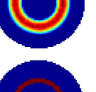
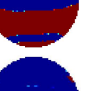




Tab.2 Image RE (%)

	LBP	TR	TSVD	ART	Landweber	ITR	Ours
a	40.81	14.33	12.27	10.18	14.38	8.37	3.95
b	36.54	19.27	17.37	13.65	15.90	12.69	8.32
c	53.55	40.27	35.85	34.43	38.15	24.80	6.12
d	36.77	25.27	28.17	22.89	19.49	31.22	9.97

Tab.3 Image CC (%)

	LBP	TR	TSVD	ART	Landweber	ITR	Ours
a	41.66	76.07	81.20	85.55	76.23	92.97	98.21
b	42.50	74.69	77.66	84.14	79.21	86.32	94.33
c	27.12	48.87	52.48	56.27	52.44	67.43	97.42
d	73.61	65.49	55.87	74.85	81.68	51.37	95.09

Tab.4 Image reconstruction results

Algorithm	a	b	c	d
LBP				
TR				
TSVD				
ART				
Landweber				
ITR				
Ours				

The first row of the table represents the original flow diagram of flow types a, b, c, and d. It can be seen from Tab.4 that the images reconstructed by the comparison algorithms all have obvious artifacts and blurred edges. For the direct algorithm, although the LBP algorithm can perform real-time imaging, the reconstructed image has

larger deformation and distortion. Although the TR algorithm can maintain the stability of the solution well, the reconstructed image is too smooth, and details are lost. Although the TSVD algorithm can be reconstructed in real time, its imaging quality is still lacking. For the iterative algorithm, the quality of the reconstructed image is generally better than that of the direct algorithm. Although ART and Landweber algorithms have low computational costs, they have no prior information support, have semi-convergence, poor image quality, and poor stability. Although the ITR algorithm has relatively good stability, the imaging is still too smooth. For the improved algorithm, although the edge information of flow types b and d will be slightly lost, the overall quality of the reconstructed image is high, the existence of artifacts is eliminated for the four flow types, the details of the reconstructed image are relatively complete, and the edges are clearer. This further proves that the improved algorithm can obtain higher-quality reconstructed images than other algorithms.

In general, the selection of distinct initial values has an effect on the outcome of picture reconstruction. At the same time, the sensitivity of the initial values of the algorithm can also be used to evaluate its performance. Therefore, in order to verify the initial value sensitivity of the algorithm, LBP, TSVD, and TR were selected as the initial values of the improved algorithm for comparison. The results are shown in Fig.2.

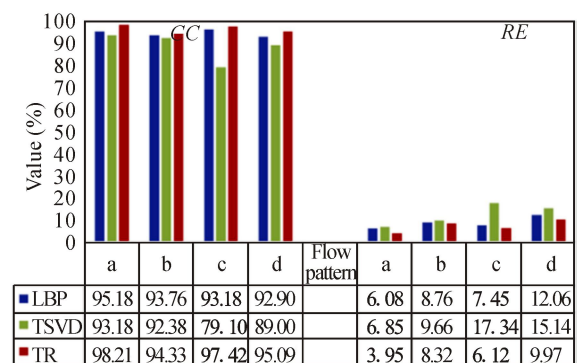


Fig.2 Comparison of different initial values

The histograms in the left and right parts of Fig.2 represent CC and RE , respectively. It can be seen from Fig.2 that although the imaging result of flow pattern c is inferior to other flow patterns when TSVD is used as the initial value, overall, the improved algorithm is less dependent on the initial value, especially for flow pattern b, where the fluctuations of CC and RE are only about 1.30% and 0.89% on average. Therefore, no matter which one of the direct algorithms is selected as the initial vector, it has high imaging quality. Thus it is proved that the improved algorithm has initial value insensitivity.

In order to verify the convergence of the improved algorithm, the result of the TR algorithm is selected as the same initialization vector. The improved algorithm is compared with the ITR algorithm for 1 000 iterations.

The results are shown in Figs.3 and 4.

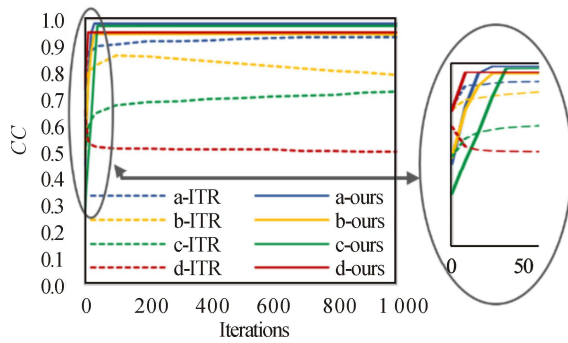


Fig.3 Comparison of CCs for each flow pattern

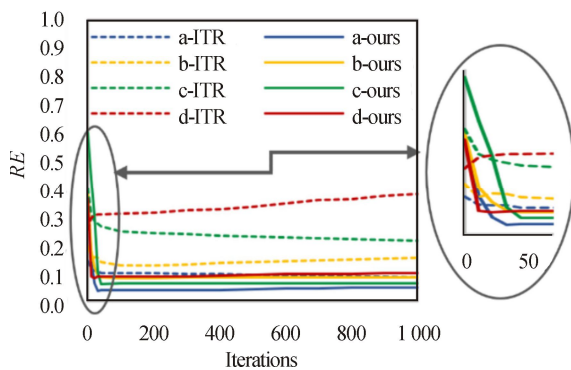


Fig.4 Comparison of REs for each flow pattern

Figs.3 and 4 show the objective quality change trend of reconstructed images using the ITR algorithm and an improved algorithm under different iteration steps and enlarge their local information. From the figure, it can be seen that the comparison algorithm ITR did not reach stable convergence with the increase of iteration steps, and even for popular b and d, CC shows a downward trend with the increase of iteration steps, and RE shows a rising trend. The improved algorithms all reach stable convergence within 50 steps, and the CC is stable above 90% and the RE is stable below 10%, which is better than the comparison algorithm. At the same time, combined with Tab.1, it can be seen that the average time for image reconstruction using the improved algorithm is 1.93 s, which is better than the ITR algorithm. Therefore, the improved algorithm can converge faster and more stably than the ITR algorithm.

The ill-posedness of ECT image reconstruction causes the reconstruction image quality to be greatly disturbed by the change in capacitance data. Therefore, in order to verify the robustness of the improved algorithm, 2%, 4%, and 6% noises were added to the capacitance data to better simulate the actual environment and test the imaging quality. The ITR algorithm and the improved algorithm were used for image reconstruction, and the comparison results are shown in Tab.5.

It can be seen from Tab.5 that the overall robustness of the improved algorithm is better than that of the ITR algorithm. With the increase in noise level, the four flow

patterns a, b, c, and d reconstructed by the ITR algorithm have obvious distortion. The three flow diagrams of a, b, and d reconstructed by the improved algorithm have no obvious distortion, and the detailed information is relatively complete. But for the c flow type, the image will be deformed to a certain extent due to its fine detail information. In order to further verify the robustness of the improved algorithm, the improved algorithm under different noise levels is compared with the objective imaging indicators of other algorithms by taking 50 averages, and the results are shown in Figs.5 and 6.

Tab.5 Image reconstruction results of each flow pattern under different noise levels

Flow pattern	Algorithm	Noise level			
		0%	2%	4%	6%
a	ITR				
	Ours				
b	ITR				
	Ours				
c	ITR				
	Ours				
d	ITR				
	Ours				

It can be seen from Figs.5 and 6 that with the increase in noise level, the objective evaluation indexes RE and CC of the image reconstructed by the improved algorithm are better than those of other comparison algorithms. For flow patterns a, b, and d, the trend graph is relatively flat. With the increase in noise level, CC can be kept relatively stable above 90% on average and RE below 10%. For flow type c, although its trend graph is not stable as the other three flow types, the improved algorithm can still maintain a higher imaging ability than other comparison algorithms. The experimental results prove that the image reconstructed by the improved algorithm is less disturbed by the capacitance data, which further verifies that the improved algorithm has better robustness.

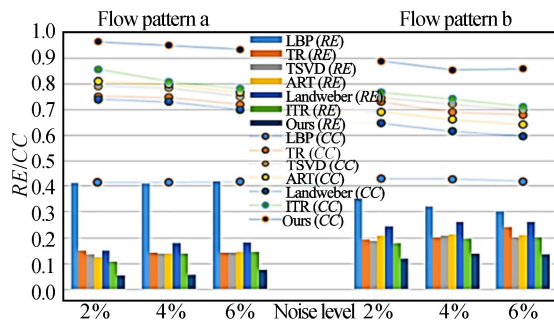


Fig.5 Flow pattern (a, b) trend chart

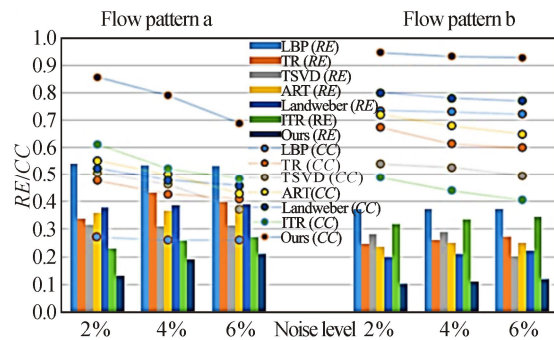


Fig.6 Flow pattern (c, d) trend chart

Aiming at the ill-posedness of ECT image reconstruction, an improved algorithm based on ITR was proposed. The experimental results show that the improved algorithm can converge more quickly and stably, with high reconstructed image quality and good initial value insensitivity and robustness.

Ethics declarations

Conflicts of interest

The authors declare no conflict of interest.

References

- [1] WANG H X. Electrical tomography[M]. 1st ed. Beijing: Science Press, 2013: 33-35. (in Chinese)
- [2] LI A Q, MENG S, HUANG K, et al. On the concentration models in electrical capacitance tomography for gas-fluidized bed measurements[J]. Chemical engineering journal, 2022, 435: 134989.
- [3] LIU J, LIU S, SUN S, et al. Internal structure visualization of flow and flame by process tomography and PLIF data fusion[J]. Journal of thermal science, 2018, 27(1): 64-73.
- [4] CARCANGIU S, FANNI A, MONTISCI A. Electric capacitance tomography for nondestructive testing of standing trees[J]. International journal of numerical modelling: electronic networks, devices and fields, 2019, 32(4): e2252.
- [5] ZHAO Y L, GUO B L, YAN Y Y. Research progress and analysis of electrical capacitance tomography[J]. Chinese journal of scientific instrument, 2012, 8: 1909-1920. (in Chinese)
- [6] ZHAO J W, YUAN Q P, QIN J, et al. Single image super-resolution reconstruction using multiple dictionaries and improved iterative back-projection[J]. Optoelectronics letters, 2019, 15(2): 156-160.
- [7] WANG H X, TANG L, YAN Y. Total variation regularization algorithm for electrical capacitance tomography image reconstruction[J]. Chinese journal of scientific instrument, 2007, 28(11): 2014-2018. (in Chinese)
- [8] HUANG D T, HUANG W Q, HUANG H, et al. Application of regularization technique in image super-resolution algorithm via sparse representation[J]. Optoelectronics letters, 2017, 13(6): 439-443.
- [9] YAN C M, MU Z, ZHANG D L, et al. ECT image reconstruction based on improved Landweber algorithm[J]. Chinese journal of sensors and actuators, 2019, 32(10): 1522-1526. (in Chinese)
- [10] TIAN Z N, GAO X X, QIU L M, et al. Experimental imaging and algorithm optimization based on deep neural network for electrical capacitance tomography for LN2-VN2 flow[J]. Cryogenics, 2022, 127: 103568.
- [11] TONG G W, LIU S, LIU S. Computationally efficient image reconstruction algorithm for electrical capacitance tomography[J]. Transactions of the institute of measurement & control, 2019, 41(3): 631-646.
- [12] LIU J, LIU S, ZHOU W, et al. Flame detection on swirl burner using ECT with dynamic reconstruction algorithm based on the split Bregman iteration[J]. IEEE sensors journal, 2017, 17(22): 7290-7297.
- [13] CUI L, TIAN P, WANG C, et al. Iterative weighted fidelity and hybrid regularization-based algorithm for ECT[J]. Measurement science and technology, 2022, 33(6): 065404.
- [14] CUI A, PENG J, LI H, et al. Iterative thresholding algorithm based on non-convex method for modified LP-norm regularization minimization[J]. Journal of computational and applied mathematics, 2019, 347: 173-180.
- [15] ZHAO Q, LIU S, CHAI X, et al. A novel computational imaging algorithm based on split Bregman iterative for electrical capacitance tomography[J]. Measurement science and technology, 2021, 32(12): 125401.
- [16] LUO Y H. Research on exponential filter in filtered back projection algorithm for CT image reconstruction[J]. Computer science, 2014, 101: 220-223.
- [17] YAN C M, MU Z. An improved gradient accelerated Landweber algorithm and its application in ECT image reconstruction[J]. Journal of electronic measurement and instrument, 2021, 35(6): 169-175.